Annals of Nuclear Energy 121 (2018) 232–249

Contents lists available at ScienceDirect

Annals of Nuclear Energy

journal homepage: www.elsevier.com/locate/anucene

Perturbation scheme for estimating uncertainties in thermal scattering cross sections of water

Lance Maul [a,*], José Ignacio Márquez Damián [b], George Braoudakis [c], Mark Ho [c], Guan Heng Yeoh [a]

[a] Australian Nuclear Science and Technology Organisation, University of New South Wales, Australia
[b] Departamento Física de Neutrones, Centro Atómico Bariloche, Argentina
[c] Australian Nuclear Science and Technology Organisation, Australia

ARTICLE INFO

Article history:
Received 3 May 2018
Received in revised form 22 June 2018
Accepted 9 July 2018
Available online 24 July 2018

Keywords:
Perturbation
Thermal scattering
Cross sections
Uncertainties

ABSTRACT

Neutron-moderator scattering interactions in the thermal energy range are often treated with specialised cross section data derived from the Thermal Scattering Law S(α,β). This scattering law is calculated based on theoretical and experimental models that describe the structure and dynamics of the principle moderator molecule. In this work, a perturbation scheme based on the Total Monte Carlo method is described and the uncertainties of the parameters used to calculate S(α,β) for H in H_2O and D and O in D_2O from the ENDF/B-VIII.0 library were estimated and propagated through to the cross sections and to an integral criticality scenario in the OPAL Reactor, Sydney Australia, using the transport code Serpent. The calculated uncertainties in the total cross sections are in reasonable agreement with experimental data and provide a basis for future model refinement; uncertainties in several parameters used in the LEAPR of NJOY were identified as critical to specific energy regions and behaviours of the total cross sections. The effect on criticality of these uncertainties was found to be 48 pcm and 41 pcm for H_2O and D_2O, respectively, within the OPAL Reactor during a low-power configuration.

1. Introduction

Neutron moderators are an important material in thermal fission reactors, providing the vast majority of the neutron thermalisation required to realise a critical system. The most typical moderators used today are overwhelmingly light (H_2O) and heavy water (D_2O), often serving as both a coolant and moderator. At lower incident energies, a neutron can interact with the molecular structure of a material as well as the nucleus of a given atom and as such, requires a specialised treatment of interaction probability; momentum and energy exchange between the water molecule and an incident neutron can take place via translation, rotation, libration and vibration of the water molecule. Using nuclear data processing codes, such as NJOY, the thermal scattering cross section of such materials is calculated from the thermal scattering law S(α,β).

Up until recently, the thermal scattering data used in the major nuclear data libraries was derived from two models: from GA model (MacFarlane, 1994) and the IKE model (Mattes, 2005) based on experimental data compiled by Koppel and Houston (1978). Now, the new evaluation ENDF/B-VIII.0 library utilises a new model for H_2O and D_2O: the Centro Atomico Bariloche (CAB) model for water (Brown et al., 2018) (Márquez Damián et al., 2014). The new JEFF-3.3 library also uses the D and O in D_2O obtained from the CAB model. This model is based on molecular dynamics (MD) data obtained using the TIP4P-2005f flexible model for water (González and Abascal, 2011) used for calculation of the continuous frequency spectrum, vibrational modes and partial structure factors (for D_2O), and experimental data from Novikov used in calculation of the diffusion parameters (Novikov et al., 1990).

While the validation of the CAB models for water look promising, an estimation of the uncertainty of the data is important. In this work we present a methodology for parameterisation of the H_2O and D_2O models and a perturbation scheme based on the Fast Total Monte Carlo (TMC) method (Rochman et al., 2014). This will allow estimates of uncertainties on successive calculated quantities using these thermal scattering cross sections as well as offer a basis for future model refinement.

2. CAB model

2.1. Key parameters of thermal scattering law models

The expression for the double differential thermal scattering cross section is given by (Parks, 1970):

* Corresponding author.
E-mail address: lancem@ansto.gov.au (L. Maul).

https://doi.org/10.1016/j.anucene.2018.07.020
0306-4549/

$$\frac{\partial^2\sigma}{\partial\Omega\partial E} = \frac{\sigma_b}{4\pi kT}\sqrt{\frac{E'}{E}}\exp\left(-\frac{\beta}{2}\right)S(\alpha,\beta) \quad (1)$$

where E and E' are the incident and secondary neutron energies, σ_b is the bound scattering cross section, kT is the temperature in eV, α is the dimensionless momentum transfer, β is the dimensionless energy transfer and $S(\alpha,\beta)$ is the symmetric form of the scattering law. The bound scattering cross section which is related to the free atom cross section by:

$$\sigma_b = \frac{(A+1)^2}{A^2}\sigma_{free} \quad (2)$$

$S(\alpha,\beta)$ can be calculated using parameters derived from a physical model of a material, typically using a nuclear data processing code such as LEAPR in the NJOY package (Muir et al., 2012). Prior to 2017, the major evaluations (e.g. ENDF and JEFF) were produced largely based on two models: the General Atomics (GA) model (up to ENDF/B-VI.8) and the IKE model (JEFF-3.2, ENDF/B-VII.1) both building primarily off the work conducted by Nelkin (1960) and Haywood and Thorson (1962). Presently, new models, called the CAB models for water, based largely on MD simulations and newer experimental data are being used in ENDF/B-VIII.0 and JEFF-3.3 (JEFF-3.3 uses only D and O in D_2O from the CAB model). Full details of the CAB models can be found in (Márquez Damián et al., 2014). Table 1 contains the key scalar parameters for these models.

In addition to the scalar parameters are three vector quantities, the alpha and beta grids and the continuous frequency spectrum (CFS). The specifics of the alpha and beta grids are not so important as to warrant comparison. The CAB model CFS for H in H_2O differs from the CFS used in previous evaluations in a few important ways: the diffusion component to be added back into the spectrum in LEAPR uses the Egelstaff-Schofield approximation (Egelstaff and Schofield, 1962), rather than the free-gas approximation; the presence of a translational mode around 6 meV represented in the CFS, experimentally observed in (Bellissent-Funel et al., 1995); a narrower rotational mode around 60 meV and an adjusted weight. Fig. 1 contains the CFS used in the last several evaluations for H in H_2O, adjusted to reflect the spectrum weights associated with each evaluation.

The CAB model for D in D_2O has similar differences with a narrower rotational band around 48 meV, the Egelstaff-Schofield diffusion model and increased weight. The IKE model used in JEFF-3.2 and ENDF/B-VII.1, however, also featured a translational vibrational mode in the CFS, in the form of a Debye distribution with a Debye temperature of ~20 meV. The CAB model for D in D_2O is used in ENDF/B-VIII.0 and JEFF-3.3. Fig. 2 contains the CFS used in the last several evaluations for D in D_2O.

The GA model assumes the scattering of D in D_2O as completely incoherent, as Koppel and Young (Koppel and Young, 1965) showed that although coherent scattering has a significant effect on the total cross section, its effect on thermalisation is of second order. The IKE model does include a structure factor for D in D_2O and uses the Sköld method to apply a coherent correction to the scattering law in LEAPR. This structure factor was obtained using a Lennard-Jones model.

In all the models discussed above, the oxygen atom in H_2O was treated as a free-gas scatterer with a mass of 16. The GA and IKE models also used a free-gas scatter for the oxygen atom in D_2O,

Table 1
Key LEAPR scalar parameters for H in H_2O and D in D_2O from the GA, IKE and CAB models.

Parameter	GA		IKE		CAB	
	H_2O	D_2O	H_2O	D_2O	H_2O	D_2O
Free-atom cross section σ_{free}	20.36b	3.37b	20.478b	3.395b	20.436b	3.395b
Diffusion weight w_d^*	0.05556	0.05	0.02174	0.05	0.007918	0.01629
Oscillator 1 energy E_1	0.205 eV	0.142 eV	0.205 eV	0.145 eV	0.205 eV	0.15 eV
Oscillator 2 energy E_2	0.48 eV	0.305 eV	0.436 eV	0.338 eV	0.415 eV	0.205 eV
Oscillator 1 wt w_1^*	0.1667	0.1667	0.1630	0.1667	0.1567	0.14293
Oscillator 2 wt w_2^*	0.3333	0.3333	0.3261	0.3333	0.3133	0.2925
Continuous spectrum weight w_β^*	0.4444	0.45	0.4891	0.45	0.5221	0.5449

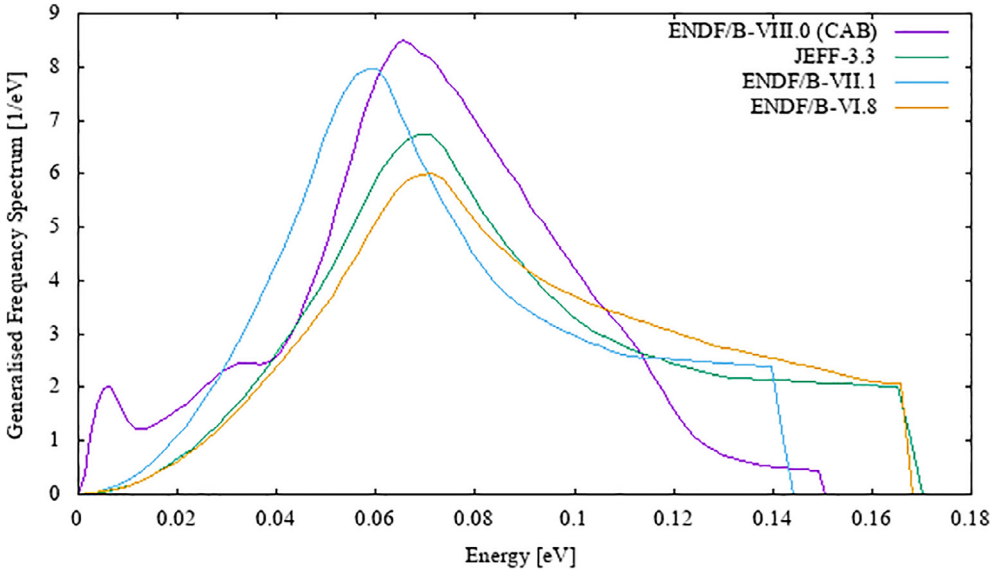

Fig. 1. CFS for H in H_2O at room temperature from previous evaluations up to the present. The CAB model is used in the ENDF/B-VII.0 evaluation.

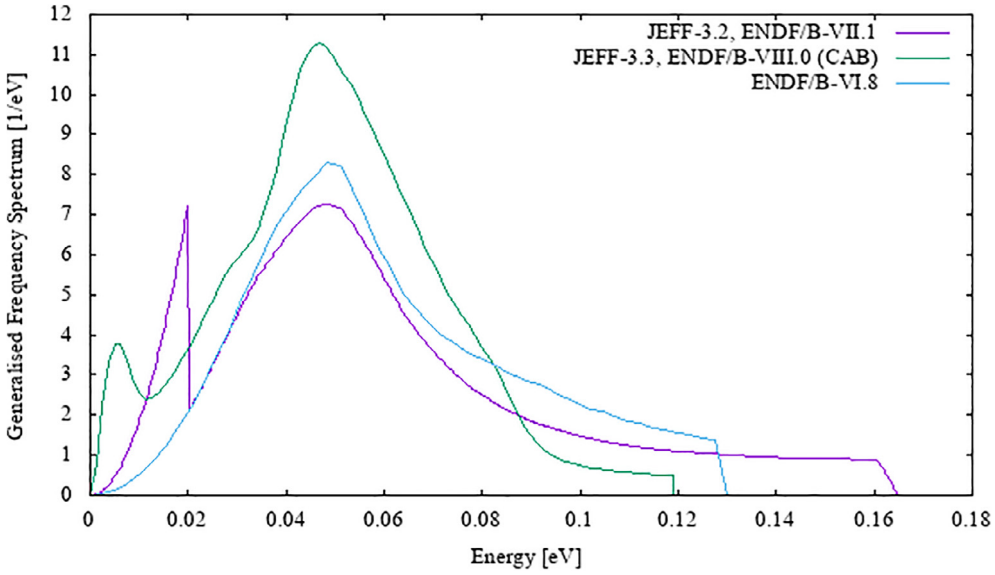

Fig. 2. GFS for D in D_2O at room temperature from previous evaluations up to the present.

but the CAB model includes parameters for an explicit scattering law of O in D_2O, including a coherent correction. This is owing to the fact that ^{16}O constitutes roughly 1/3 of the thermal scattering cross section over much of the thermal range.

2.2. Details of CAB models for water

Fig. 3 shows the cross section of ^{1}H using both the free-gas model and the CAB thermal scattering model, highlighting the disparity between the two results, particularly around the 25.3 meV range.

The generalised frequency spectrum for each material was calculated using MD simulations. From the generalised spectrum, the diffusion components were removed from the lower energies and truncated after the rotational band, cutting off the vibrational peaks contributed by the O—H (or O-D) bond stretching and bending modes; this resulting spectrum is referred to in this text as the continuous frequency spectrum (CFS) and contains the hindered rotational modes as well as stretching and bending of the hydrogen bond network.

In LEAPR, the scattering law computed from the CFS by phonon expansion is convolved with the scattering law from discrete oscillators and the diffusive scattering law using the Egelstaff-Schofield model to realise the description of the dynamics of the molecule in the incoherent approximation.

In the case of D and O in D2O, a coherent correction is applied using the Sköld model (Sköld, 1967):

$$\begin{aligned} S(\alpha,\beta) &= (1-c_{frac})S_{inc}(\alpha,\beta) + c_{frac}S_{coh}(\alpha,\beta) \\ &= (1-c_{frac})S_{inc}(\alpha,\beta) + c_{frac}S_{inc}(\alpha/S(Q),\beta)S(Q) \end{aligned} \quad (3)$$

where $c_{frac} = \sigma_{coh}/(\sigma_{coh}+\sigma_{inc})$ is the coherent fraction, and $S(Q)$ is the Sköld correction function. The Sköld correction functions for D and O in D_2O are given in the polyatomic approximation (Vineyard, 1958) by:

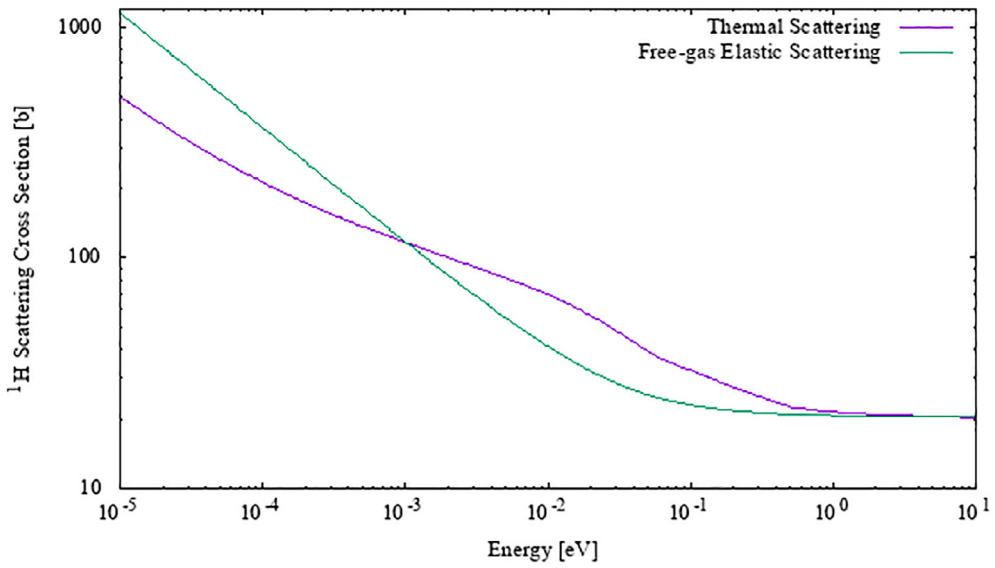

Fig. 3. Scattering cross section of ^{1}H using the free-gas and CAB thermal scattering models.

$$S_D(Q) = 1 + \frac{2}{3}(S_{DD}(Q) - 1) + \frac{1}{3}\frac{b_O}{b_D}(S_{OD}(Q) - 1) \quad (4)$$

$$S_O(Q) = 1 + \frac{1}{3}(S_{OO}(Q) - 1) + \frac{2}{3}\frac{b_D}{b_O}(S_{OD}(Q) - 1) \quad (5)$$

where b_D and b_O are the coherent scattering lengths for D and O, and S_{DD}, S_{OD}, S_{OO} are the partial structure factors for deuterium-deuterium, oxygen deuterium and oxygen-oxygen correlations. The partial structure factor for each atom-pair is computed from the radial Fourier transform of the radial distribution function (RDF) $g(r)$ obtained from MD simulations:

$$S_{XX}(Q) = 1 + 4\pi\rho\int_0^\infty r^2(g_{XX}(r) - 1)\mathrm{sinc}(Qr)dr \quad (6)$$

where S_{XX} and g_{XX} are the partial structure factors and RDFs for OO, OD or DD, r is the pair-pair distance, Q is the change in wavenumber of the neutrons and ρ is the atomic density of the material.

3. Perturbation scheme

3.1. Fast TMC method

The Total Monte Carlo (TMC) method provides researchers with a simple and robust way of propagating uncertainties from nuclear data parameters to cross section or integral quantities in transport calculations. This is achieved by sampling from distributions about the nominal value of input parameters characterised by their uncertainty. Then, using these perturbed parameters, a set of data can be produced and their variance calculated. The major drawback of this approach is the typically high computational requirement, with at least hundreds of iterations required to obtained a sample of the population of the quantities of interest. This limitation is not a concern in short, deterministic calculations, such as processing cross sections, but for Monte Carlo transport problems, it can become an intractable limitation.

Rochman et al. (2014) proposed a modified approach to the original Total Monte Carlo (TMC) method to improve the efficiency of the process by greatly reducing the computational power required. The Fast TMC method capitalises on the use on the Monte Carlo method already employed in transport calculations. While the original method would call for n unique calculations, using a single seed, with sufficiently small statistics to justifiably quantify propagated uncertainties, the Fast TMC approach utilises a unique seed for each calculation, thereby reducing the number of histories required to realise a satisfactory estimate of the sensitivity of the quantity of interest.

The uncertainty induced onto the quantity of interest is given by:

$$\sigma_{XS} = \sqrt{\sigma_{obs}^2 - \overline{\sigma}_{stat}^2}, if\ \frac{\sigma_{stat}}{\sigma_{obs}} \leq 0.5 \quad (7)$$

where σ_{obs} is the standard deviation of the distribution of calculated values of the quantity of interest and $\overline{\sigma}_{stat}$ is the average statistical error associated with the calculated quantity. As statistical errors are often underestimated for calculated quantities in MC codes, a true estimate of the statistical error can be obtained by running many identical calculations using a unique seed, referred to in this text as $\sigma_{unbiased}$. The condition that the ratio of the statistical and observed error is <0.5 is not rigorous, but serves as a rough guide. If the ratio were to exceed this value, then the statistical error dominates the total error of the distribution and should probably be rejected. It is also important to check for normality in the calculated distribution - deviation from normal will likely obfuscate the induced error.

The perturbation can be broken up into two stages. First, a set of 486 thermal cross section files was generated each for H in H_2O and D & O in D_2O. Each input parameter was assigned a random value sampling from an associated uncertainty. Except for the alpha and beta grid variables (further discussed in Section 3.2.3), all quantities were perturbed by sampling from the standard Gaussian distribution (mean = 0, σ = 1) and multiplying by the applicable uncertainty. 5 key scalar quantities were sampled orthogonally from this distribution, discussed further in Section 3.2.1. This is essentially a Latin Hypercube sampling, except that the subdivisions of the sampling space for each set of quantities is permutated so as to provide a more even sampling of the whole sample space, e.g. if two quantities were to be sampled with two subdivisions of the sample space in each quantity, orthogonal sampling will ensure that each permutation of the sampling of these two quantities sample a unique combination of subdivisions, resulting in four permutations. This orthogonal sampling provides a better estimate of the variability of the of these parameters. In this work, the range of each random variable was subdivided into 3 equi-probable intervals, resulting in 243 permutations, namely σ_{free}, w_d, c, E_1 and E_2. Each permutation was sampled twice, providing 486 parameter sets. Three of these sets were produced and one used each for H in H_2O, D in D_2O and O in D_2O. The remaining random variables were just sampled from the standard Gaussian distribution, with the exception of the perturbation of the α/β grids, which used a uniform distribution.

From these perturbed cross section files, the uncertainties in total cross section could be calculated as well as co-variances between several quantities, such as the covariance matrix associated with the cross section data itself and covariances between model parameters and the total cross section.

The second stage was propagating the uncertainties in the LEAPR parameters through to Serpent (Leppänen et al., 2015), in which the Fast TMC method was used. 486 unique thermal cross sections for each H in H_2O, and D and O in D_2O were run, with either a perturbed H or D and O file used in a single calculation. Care was taken to randomise the pairing of the perturbed D and O cross sections to mitigate any correlation created by the use of orthogonal sampling of the creation of the cross sections. Based on preliminary estimates of the propagated uncertainty onto k_{eff} in the OPAL reactor model, each calculation ran enough neutron histories to achieve a statistical uncertainty of ~10 pcm.

A separate set of 200 Serpent calculations was run using unperturbed cross sections with unique seeds and using the same number of neutron histories. From this a distribution for each quantity of interest was obtained to provide an unbiased estimate of the statistical uncertainty. Quantities of interest include k_{eff}, and detector tallies in various positions of the OPAL reactor.

3.2. LEAPR parameters

The LEAPR module of NJOY is used to calculate the thermal scattering law and requires several input parameters, which will be broken down into four sections:

- Scalar quantities
- CFS $\rho(\beta)$
- Momentum (α) and energy (β) grids
- Structure correction functions $S(Q)$

The scalar quantities are straight forward to perturb and uncertainties are taken or estimated from experimental data. The latter three quantities are vectors and as such the perturbation method is more involved.

3.2.1. Scalar quantities

The nominal values and estimated uncertainties for each of the scalar quantities are taken directly from the CAB model used in the ENDF/B-VIII.0 library and are shown in Table 2, unless otherwise stated below. The term uncertainty in this work refers to the standard deviation of the quantity.

The free-atom cross section uncertainties were obtained from the EXFOR database. The diffusion constants were estimated based on measurements of the self-diffusion coefficients in water by Yoshida et al. (2008). The oscillator energy uncertainties were estimated from the infrared spectra measurements of Lappi et al. (2004). The coherent scattering fraction uncertainty in D in D_2O was obtained ad hoc, providing a total sample range of ~ ±1%. The continuous weight w_β uncertainty was not sampled directly. Typically the area under the spectrum serves as the weight (i.e. the spectrum is normalised with respect to the sum of all weights) and thus w_β was calculated directly from the perturbation of the CFS itself (Section 3.2.2). The oscillator weights were calculated:

$$w_1 = \frac{1}{3}(1 - w_d - w_\beta) \tag{8}$$

$$w_2 = \frac{2}{3}(1 - w_d - w_\beta) \tag{9}$$

The distribution of the derived w_β, w_1 and w_2 were examined for each cross section set and found to be Gaussian in nature. In the case of O in D_2O, the nominal values for w_d and w_β sum to ~0.885, creating a large uncertainty for the oscillator weights. This large uncertainty is clearly an overestimation with respect to the physical model used for O in D_2O, but appears to have negligible impact on cross section calculations, as reported in Section 5.

3.2.2. Continuous frequency spectrum

The CFS in the CAB models for water was calculated by taking the cosine Fourier transform of the velocity autocorrelation function (VACF) obtained from MD calculations. Novikov proposed the parameterisation of the spectrum by use of the sum of fitted Gaussian distributions (Novikov et al., 1990). While not a true representation of the physics of the constituent modes of excitation of the water molecule, this approach provides a strong approximation to it and an easy start point for perturbation. Initially, five Gaussian distributions were used to reconstruct the CFS for each material. A sixth was added as an auxiliary to the tail of the reconstruction to better replicate the spectrum used in the CAB models.

An estimation of the uncertainty was calculated by using the same reconstruction technique applied to another CFS calculated using a different MD model for water (Marquez Damian et al., 2013), namely SPC-MPG (Marti et al., 1994). The reconstructed spectra from the CAB model and the SPC model were iterated 3 times between each to minimise the differences in the Gaussian parameters, then the difference was calculated for each parameter. This calculated difference served as the uncertainty for each parameter of the CAB model spectrum. While this approach can certainly reproduce both spectra to within an acceptable error of the original, by sampling from this distribution, unphysical results can be produced. This was minimised by designating each calculated parameter uncertainty described above as a 3σ error. It should also be noted that a given parameter set that produces a good approximation to the original spectrum is not unique and that sampling hundreds of perturbed spectra from two faithful reconstructions will likely give tangibly different results. The reconstructed spectrum is given by:

$$\rho(E) = \sum_{n=1}^{6} \frac{w_n}{2\pi\sigma_n^2} \exp\left(-\frac{(E-\mu_n)^2}{2\sigma_n^2}\right), \quad \{E|0 \le E \le 150meV\} \tag{10}$$

The energy grid for the continuous spectrum uses an interval of 0.1265 meV. The continuous spectrum weight was calculated by numerical integration under the curve using the trapezoidal rule. The first two points on the spectrum was also adjusted to ensure a value of 0.0 for the first point and a smooth transition up to the first peak. The fitting was based on the gradient of the original CFS in this region.

The nominal parameters for each Gaussian distribution are given in Tables 3–5.

The thermal cross section produced from a thermal scattering law file is sensitive to structure of the lower energy region of the CFS, so care was taken to minimise the error to as high an energy as possible. For each spectra reconstructed, the relative error of reconstruction was <2% until after the rotational peak of each spectra where the CFS values are lower and of far lesser importance to the calculation of the scattering law. The relative error in the integral of each CFS is <1%. The reconstruction of the H in H2O CFS is shown in Figs. 4 and 5 contains the relative errors of each reconstructed CFS.

3.2.3. Alpha/Beta grids

The successful meshing of the alpha and beta grids are tied to the structure of the CFS and it is not clear how to accurately construct or indeed perturb the grid. As the CFS is altered in a given iteration, it is not clear how to provide optimised alpha and beta grids. Instead, an envelope function was applied to the existing grids for each material designed to modulate the spacing between each point about a randomly sampled point. The envelope function and adjusted grid point are given by:

$$F(A_G, w, x_0, x) = \frac{A_G}{2}\left(\cos\left(\frac{\log(x)\pi}{w}\right) + 1\right)(\log(x) - x_0), (x_0 - w, x_0 + w) \tag{11}$$

$$\log(x') = F(A_G, w, x_0, x) + \log(x) \tag{12}$$

Table 2
CAB model LEAPR parameters and uncertainties.

Parameter	H in H_2O		D in D_2O		O in D_2O	
	Value	Uncertainty	Value	Uncertainty	Value	Uncertainty
Free-atom cross section σ_{free} †	20.43608b	±0.41%	3.395b	±1.6%	3.7939b	±1.6%
Diffusion constant c†	3.969	±2.5%	3.1934	±2.53%	3.1639	±2.53%
Diffusion weight w_d *,†	0.007918	±2.5%	0.016293	±2.5%	0.1306	±2.5%
Oscillator 1 energy E_1 †	0.205 eV	±2.1%	0.15 eV	±3.0%	0.15 eV	±3.0%
Oscillator 2 energy E_2 †	0.415 eV	±3.7%	0.205 eV	±6.2%	0.205 eV	±6.2%
Oscillator 1 wt w_1 *	0.15667	±1.9%	0.14293	±3.9%	0.038288	±23.5%
Oscillator 2 wt w_2 *	0.31333	±1.9%	0.29254	±3.9%	0.076576	±23.5%
Continuous spectrum weight w_β *	0.52208	±1.7%	0.5449	±3.2%	0.75454	±3.8%
Coherent scattering fraction σ_{coh}/σ	n/a	n/a	0.7319	±0.3%	1	0%

* These values sum to a total 1 for each iteration.
† These values were sampled orthogonally during the perturbation.

Table 3
CAB model CFS reconstruction parameters for H in H_2O.

G_n	Mean [eV]	Uncertainty	σ [eV]	Uncertainty	Weight	Uncertainty
G_1	0.0055	±3.0%	0.00305	±4.9%	0.0121	±3.3%
G_2	0.0159	±6.0%	0.0074	±1.1%	0.0207	±24.8%
G_3	0.0305	±1.0%	0.0069	±8.2%	0.0297	±13.2%
G_4	0.0634	±4.7%	0.0144	±3.7%	0.244	±1.0%
G_5	0.0922	±2.7%	0.0192	±3.1%	0.21	±2.9%
G_6	0.147	±1.0%	0.012	±11.1%	0.012	±13.9%
Area	0.5214					

Table 4
CAB model CFS reconstruction parameters for D in D_2O.

G_n	Mean [eV]	Uncertainty	σ [eV]	Uncertainty	Weight	Uncertainty
G_1	0.0052	±1.0%	0.0028	±1.2%	0.0195	±5.1%
G_2	0.0151	±5.5%	0.00785	±4.5%	0.0416	±13.9%
G_3	0.0284	±2.0%	0.066	±1.0%	0.0612	±3.4%
G_4	0.0449	±3.4%	0.0079	±8.9%	0.1465	±9.2%
G_5	0.0616	±1.4%	0.0138	±3.1%	0.231	±1.9%
G_6	0.0922	±7.5%	0.0424	±1.0%	0.0645	±5.9%
Area	0.5420					

Table 5
CAB model CFS reconstruction parameters for O in D_2O.

G_n	Mean [eV]	Uncertainty	σ [eV]	Uncertainty	Weight	Uncertainty
G_1	0.00485	±1.4%	0.0024	±2.8%	0.13	±6.4%
G_2	0.0075	±5.8%	0.0034	±1.5%	0.1055	±8.4%
G_3	0.0155	±1.7%	0.005	±3.3%	0.14	±11.7%
G_4	0.0266	±1.3%	0.006	±1.1%	0.226	±11.1%
G_5	0.04	±1.9%	0.0122	±3.3%	0.0851	±7.4%
G_6	0.0645	±1.8%	0.0188	±2.3%	0.081	±1.6%
Area	0.7551					

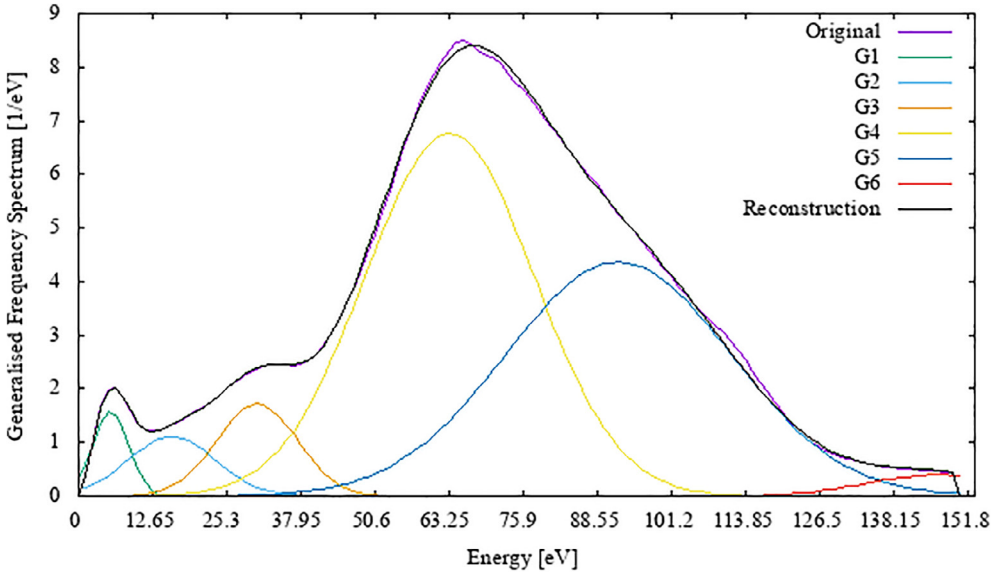

Fig. 4. Original ENDF-B-VIII.0 and reconstructed CFS for H in H2O, with constituent Gaussian functions.

where A_G is the grouping coefficient, used to determine the extent of the modulation of point spacing, x_0 is the origin on the envelope and w is the width of the envelope. These three parameters were randomly sampled for each iteration of the cross section generation. Essentially, the function behaves analogous to placing a magnifying lens over the points, with the sign of the A_G determining whether the transform is concave or convex. The domain of the input parameters was restricted to prevent adjustment of the first and last points on a given grid and that no point was moved outside of the existing limits of the grid. Fig. 6 shows an example of how the function behaves on equi-spaced points on a log scale. These three parameters were sampled from a uniform distribution, as a Gaussian sampling does not hold as physical significance here. As the alpha and beta grids are tied to the meshing and features of the

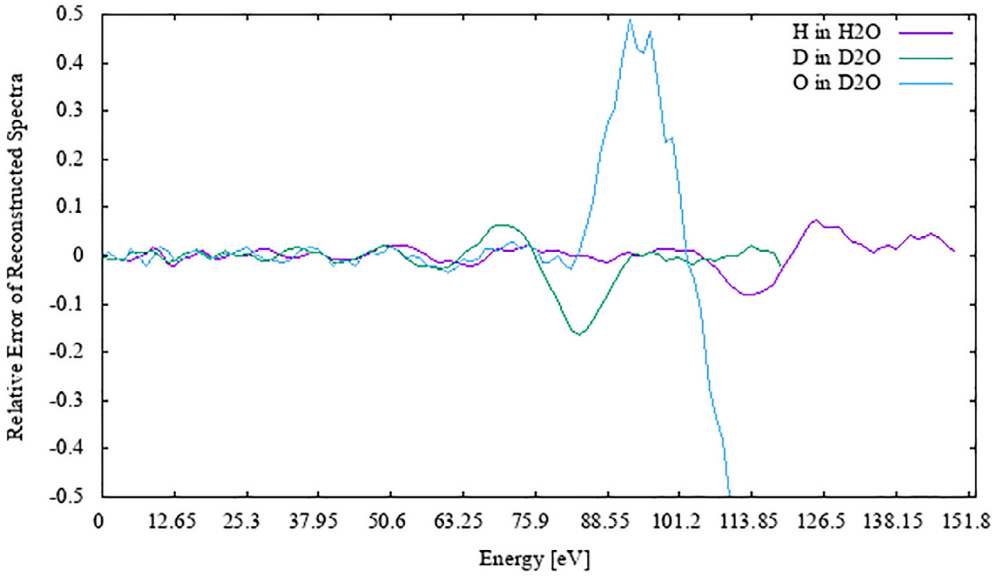

Fig. 5. Relative errors of the reconstruction of each CFS.

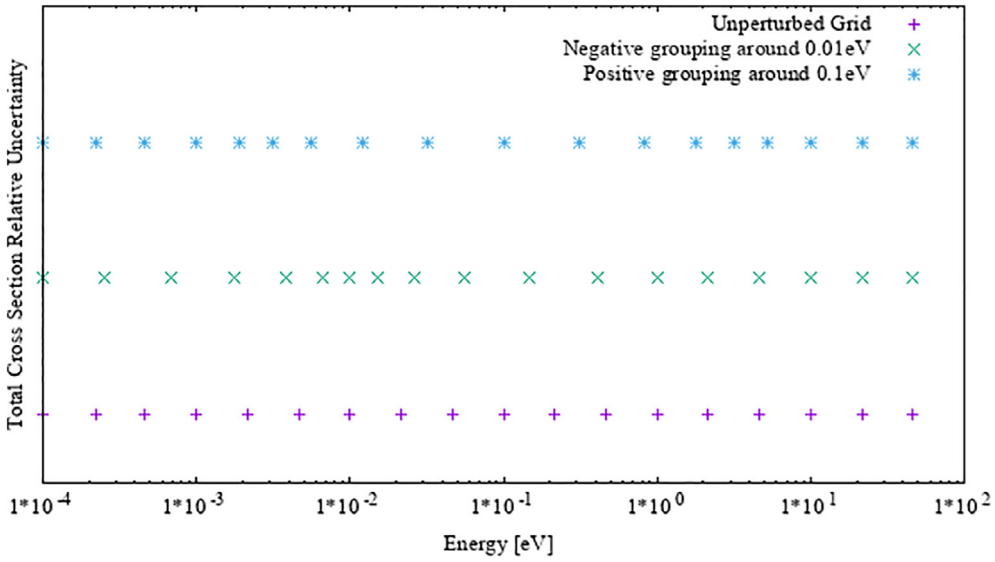

Fig. 6. Application of the envelope function for perturbing the alpha and beta grids of the LEAPR input file. The y-axis values are arbitrary and serve only to demarcate the three example groupings.

CFS, it is difficult to quantify the specific effects of perturbing the grid; a further analysis outside the scope of this work would involve adjusting the grid specifically to a constrained set of CFS parameters and the spacing and position of grid points analysed specifically.

3.2.4. Structure correction

The coherent scattering fraction of D in D_2O and O in D_2O are significant and an adjustment to the incoherent approximation used in NJOY is required for acceptable accuracy in these thermal scattering laws. The CAB models for D in D_2O and O in D_2O use the Sköld correction factor which requires the partial structure factor $S_{XX}(Q)$ for the material to be provided. Rather than perturbing $S_{XX}(Q)$ directly, the RDF for each pair-pair group (DD, OD and OO) was parameterised in a similar fashion to the CFS parameterisation. This took place in two distinct parts of the RDF: $g(r)$ was reconstructed using a combination of skewed Gaussian distributions and an exponential function up to a cut-off distance r_C given by:

$$g(r) = \sum_{n=1}^{N} \frac{w_n}{2\pi\sigma_n^2} \exp\left(-\frac{(r-\mu_n)^2}{2\sigma_n^2}\right)\left(1+\operatorname{erf}\left(\gamma_n \frac{r-\mu_n}{\sqrt{2}}\right)\right) + E(r), \quad \{r|0 \le r < r_C\} \tag{13}$$

where γ is the skew of the distribution and the $E(r)$ is given by:

$$E(r) = 1 - \exp(\zeta(r-r_0)), \quad \{r|r_0 \le r\} \tag{14}$$

where ζ is the decay constant of the exponential function and r_0 is the starting distance of the exponential function. After the cut-off, the function assumes the form of an exponentially decaying cosine function, given by:

$$g(r) = \frac{w_{e,n}}{r} \exp(-\zeta_e r)\cos(\omega r + \phi) + 1, \quad \{r|r_C \le r\} \tag{15}$$

where w_e is the amplitude of the function, ζ_e is the decay constant, ω is the angular frequency and ϕ is the phase of the cosine function. The estimates from uncertainties were derived in a similar fashion to the CFS uncertainties. Experimental data for each pair-pair $g(r)$

from Soper and Benmore (2008) was also reconstructed using this parameterisation scheme and the differences between each parameter served as a 3σ error. $S_D(Q)$ and $S_O(Q)$ were calculated according to Eqs. (4) and (5). Tables 6–9 contain the estimated uncertainties for the RDFs of the DD, OD and OO pairs. No correlations between the Gaussian parameters were taken into account.

The calculation of the low Q region of the partial structure factors was found to be extremely sensitive to seemingly imperceptible changes in the RDF. As this region does effect the total cross section of D_2O appreciably owing to the predominance of coherent scattering in D_2O, the uncertainty induced as a result of the low Q region of $S(Q)$ is considerable. Fig. 7 contains the D and O in D^2O structure corrections $S(Q)$ and Fig. 8 contains the relative error of the reconstructed $S(Q)$ with respect to the original $S(Q)$.

3.3. Calculation line

3.3.1. NJOY

The thermal cross section files were calculated using NJOY2012. upcab51, a version of NJOY that accurately reproduces the CAB models for water thermal scattering laws. A wrapper script was written to sample values for each input parameter, generate an input file for NJOY, execute NJOY, calculate a total cross section for the relevant molecule (H_2O or D_2O) and compare them to experimental data obtained from EXFOR. Severe outliers were discarded and the process repeated, though this only occurred in 4 instances of the 1458 thermal files generated. All free-gas cross sections were generated using the ENDF/B-VIII.0 library data at 300 K and all thermal cross sections were generated at 293.6 K with 32 angular bins and 500 energy bins.

3.3.2. Serpent

The second stage of this work was to propagate the uncertainties through to a Serpent model of the OPAL Reactor. The version of Serpent used was 2.1.22. Each run used 800 active cycles with an additional 100 inactive cycles and 128,000 neutron histories per cycle. Source convergence was checked by observing the Shannon Entropy over the core. Each run was furnished with an explicit randomised seed to ensure compliance with the Fast TMC method (it should be cautioned that submitting jobs in rapid succession

Table 6
CAB model RDF Gaussian reconstruction parameters for DD in D_2O.

G_n	Mean [Å]	Uncertainty	σ [Å]	Uncertainty	Weight	Uncertainty	Skewness	Uncertainty
G_1	1.5206	±0.2%	0.0785*	±14.6%*	0.52	±1.3%	1.9	±0.9%
G_2	2.127	±1.2%	0.336	±5.6%	0.641	±0.1%	3.9	±12.8%
G_3	3.698	±0.7%	0.365	±2.5%	0.377	±1.1%	0	n/a
G_4	4.605	±0.3%	0.375	±7.1%	0.137	±5.1%	0	n/a
G_5	5.944	±1.9%	0.6603	±12.1%	0.0608	±16.0%	0	n/a
G_6	7.527	±0.6%	0.5781	±4.5%	0.0409	±4.0%	0	n/a

* Due to the narrow peak of the CAB model and shallow peak of the experimental data, the nominal value of the first Gaussian σ was adjusted to the midpoint in between the two for the purposes of perturbation. The uncertainty associated with this parameter is 1/6 of the difference.

Table 7
CAB model RDF Gaussian reconstruction parameters for OD in D_2O.

G_n	Mean [Å]	Uncertainty	σ [Å]	Uncertainty	Weight	Uncertainty	Skewness	Uncertainty
G_1	0.965	±0.2%	0.0475*	±19.3%*	2.545	±1.2%	0	n/a
G_2	1.7	±1.0%	0.246	±7.3%	0.581	±0.6%	12	±13.9%
G_3	2.34	±0.0%	0.15	±0.0%	0.0172	±0.0%	0	n/a
G_4	2.95	±0.5%	0.38	±2.6%	0.6952	±0.7%	4.3	±11.6%
G_5	3.7	±0.7%	0.787	±4.5%	0.6482	±0.8%	0	n/a
G_6	5.32	±1.6%	0.3	±33.3%	0.045	±28.1%	0	n/a

* Due to the narrow peak of the CAB model and shallow peak of the experimental data, the nominal value of the first Gaussian σ was adjusted to the midpoint in between the two for the purposes of perturbation. The uncertainty associated with this parameter is 1/6 of the difference.

Table 8
CAB model RDF Gaussian reconstruction parameters for OO in D_2O.

G_n	Mean [Å]	Uncertainty	σ [Å]	Uncertainty	Weight	Uncertainty	Skewness	Uncertainty
G_1	2.664	±0.4%	0.207	±6.9%	0.992	±4.1%	14.2	±9.9%
G_2	3.135	±1.8%	0.301	±2.9%	0.286	±5.2%	0	n/a
G_3	3.845	±0.4%	0.26	±2.6%	0.088	±17.8%	0	n/a
G_4	4.38	±0.2%	0.45	±6.3%	0.43	±6.8%	0	n/a

Table 9
CAB model auxiliary reconstruction parameters for each pair-pair group.

Parameter	DD		OD		OO	
	Value	Uncertainty	Value	Uncertainty	Value	Uncertainty
τ	0.6988	±0.2%	0.9958	±0.1%	1.0334	±1.1%
r_0	1.7622	n/a	2.9	n/a	2.951	n/a
r_c	8.25	n/a	6.5	n/a	5.1	n/a
w_e	2.14	±4.0%	14.7	±24.3%	18.8	±16.8%
τ_e	0.383	±3.2%	0.586	±7.7%	0.57	±7.0%
ω	0.3285	±0.4%	0.3615	±0.0%	0.4245	±0.2%
ϕ	0.467	±1.6%	0.319	±5.9%	0.082	±23.2%

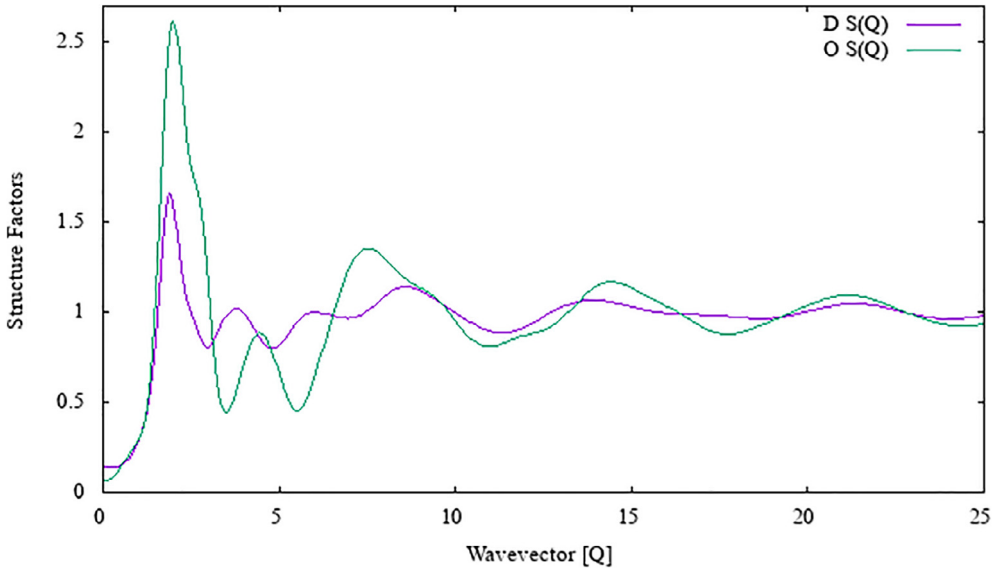

Fig. 7. Structure correction functions used for D and O in D_2O.

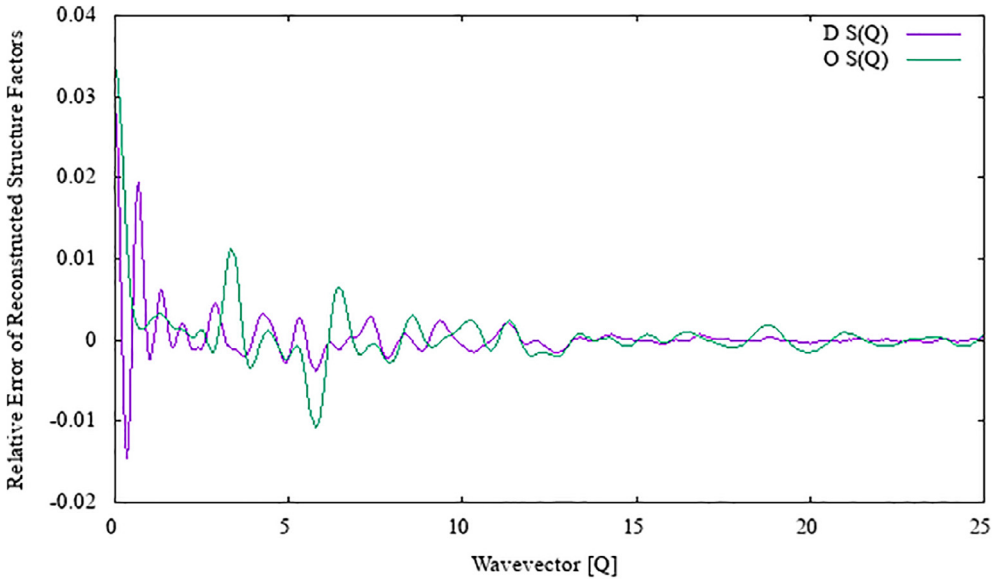

Fig. 8. Relative error of the reconstruction of the structure correction functions used for D and O in D_2O.

without setting the seed may produce several runs with the same seed as the seed is sampled from the clock). With the exception of the seed and thermal files used, the input was the same for each run. Using 16 cores @ 2.5 GHz each, each run took approximately 7.5 h to complete with a reported statistical uncertainty of k_{eff} averaging 10 pcm.

4. OPAL model

4.1. Description of the OPAL Reactor

The OPAL Reactor is a 20 MW(th) open-pool type Research Reactor located at Lucas Heights, Sydney, Australia, commissioned in 2006 (Braoudakis, 2015). The reactor has four primary objectives: production of medical radio-isotopes, materials irradiation and science, silicon neutron transmutation doping (NTD) and neutron science. The facilities that populate the heavy water (HW) reflector vessel include a cold neutron source (CNS), 36 irradiation facilities, 6 NTD facilities and 5 neutron beam lines. The core contains 16 fuel assemblies, each containing 21 aluminium fuel plates with 19.75% ^{235}U enriched U_3Si_2 fuel and 20 burnable Cd wires. The core is cooled and moderated with light water (LW) and reactivity is controlled by 5 Hf control blades: 4 plate-type absorbers located between each quadrant of the core and a central cruciform absorber used for fine control of reactivity. The core has a square cross section approximately 35 cm in length and the cylindrical HW reflector vessel is 2.6 m in diameter. The reactor operates on a ~30–35 day cycle regime, with typically 3 fresh fuel assemblies loaded in between cycles. Fig. 9 shows a 2D radial view of the core and reflector at the core-centreline, visualised using the Serpent geometry plotting utility.

4.2. Model specification

The specific configuration of the OPAL reactor used in this work is taken from the International Atomic Energy Agency (IAEA)

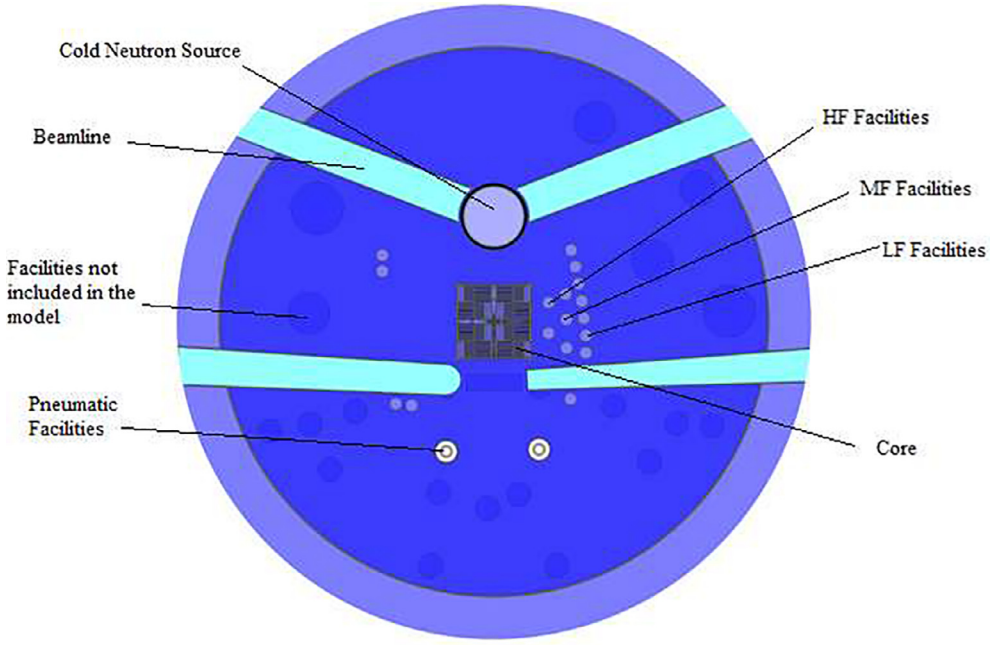

Fig. 9. Radial view of the reflector vessel, as visualised by Serpent.

Collaborative Research Project (CRP) 1496. The core is loaded with a full fresh fuel loading which features 3 types of fuel assembly: 7 assemblies with a reduced U loading of 212 g and no burnable absorber, 6 assemblies with a reduced U loading of 383 g and the remaining 3 assemblies with a full U loading of 484 g. All the irradiation facilities in the core are empty (filled with water or nitrogen) and the control rod configuration is similar to one used for operation. The system is critical. The reported power of the reactor in this configuration was 36 ± 6 kW and the moderator temperatures (LW and HW) were reported at 293 K. The outer reflector vessel facilities were not included in the model, owing to their negligible impact on the system.

5. Results and discussion

5.1. Verification of reconstructed cross sections

For the perturbation scheme to provide a reasonable estimate of the uncertainty associated with each thermal cross section generated, the parameters used to reconstruct the model must replicate the original cross section with accuracy. Most of the scalar parameters are a trivial issue as they are simply lifted from the original evaluation and perturbed, however the vector and vector-derived scalar quantities are not an exact replication of the original data. The reconstructed cross sections maintained a relative error of

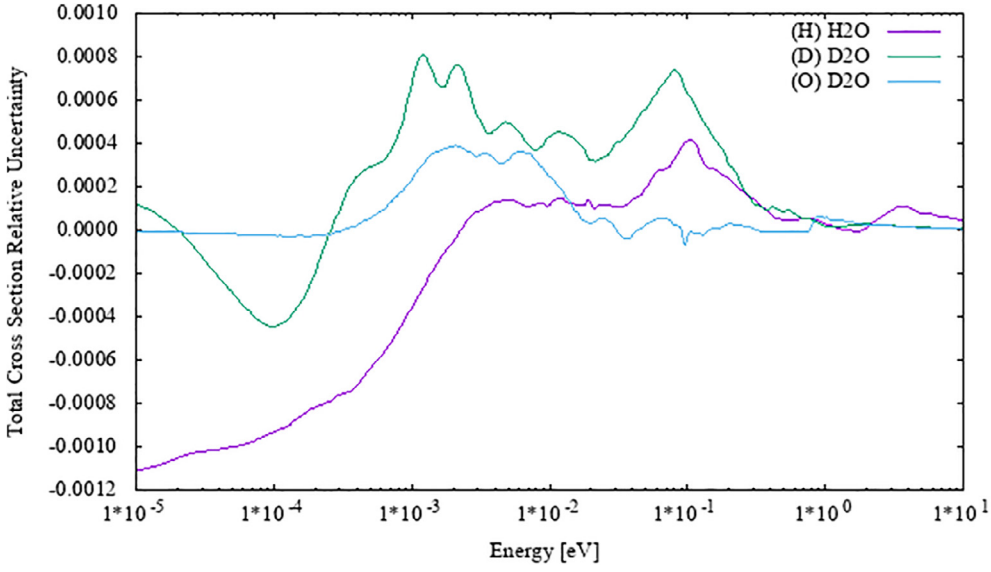

Fig. 10. Relative errors of reconstructed total cross section of H in H_2O and D & O in D_2O.

<0.1% across the entire thermal cross section energy range, with the except of H in H2O in the very cold neutron range (<50 μeV). Fig. 10 contains the relative error of each reconstruction cross section without perturbation with respect to the original.

5.2. Uncertainties in calculated cross sections

5.2.1. Uncertainty in total cross section

The uncertainty obtained from the perturbed cross sections was calculated at each point as the standard deviation of values. This is compared to the experimental cross section uncertainty for H_2O and D_2O in Figs. 11–13. In the cases of D and O in D_2O, a separate set of cross sections were generated without perturbation of the structure factor $S(Q)$. It was suspected that the uncertainty contribution of $S(Q)$ would be substantial given its extreme sensitivity at low Q to the perturbations of the RDF. The experimental data was obtained from the EXFOR database: for H_2O, the uncertainty was selected from datasets by Heinloth (1961), Russell et al. (1966), Dritsa and Kostikas (1967) and Zaitsev et al. (1991); for D_2O, the uncertainty was selected from datasets by Marquez Damian et al. (2015), Kropff et al. (1975) and Dritsa and Gaitanis (1967).

The calculated uncertainty obtained from the perturbed H_2O cross sections is underestimated with respect to the 0.1–10 meV region and the >0.5 eV region. A slight overestimation is present around the 293 K flux peak region; this is the result of a few key parameters, such as the position of the rotational band peak and the size of the hindered translation modes in the CFS and the energy of the 2nd vibrational mode; this is discussed in Section 5.2.2. The underestimated regions are not of high concern, owing to the fairly conservative estimates of the uncertainties, particularly in the higher energies where the free-atom cross section dominates the calculated uncertainty and is known with greater accuracy than the total H_2O cross section in that range. The profile of the calculated uncertainty is also quite similar to that reported

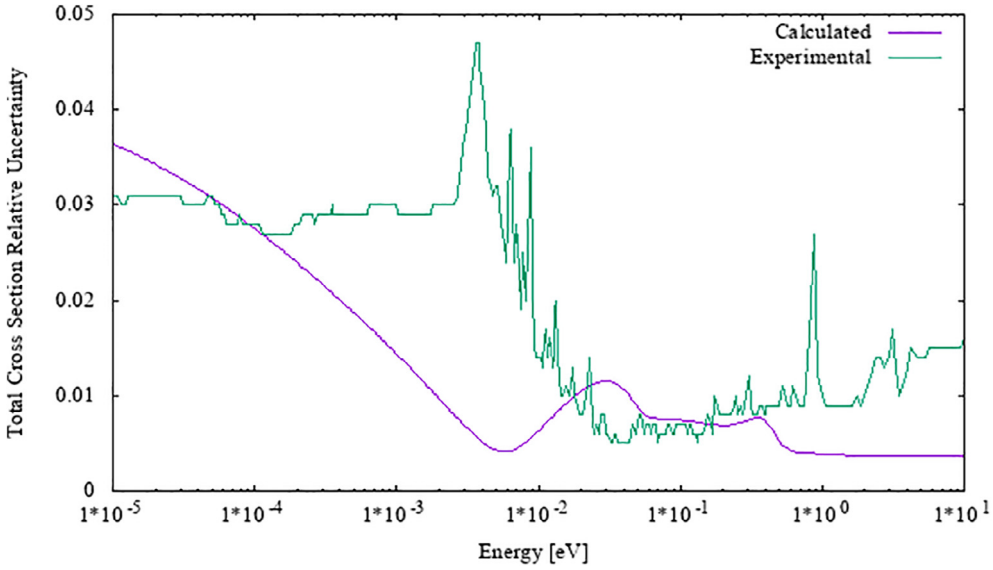

Fig. 11. Experimental and calculated uncertainty for the total cross section of H_2O.

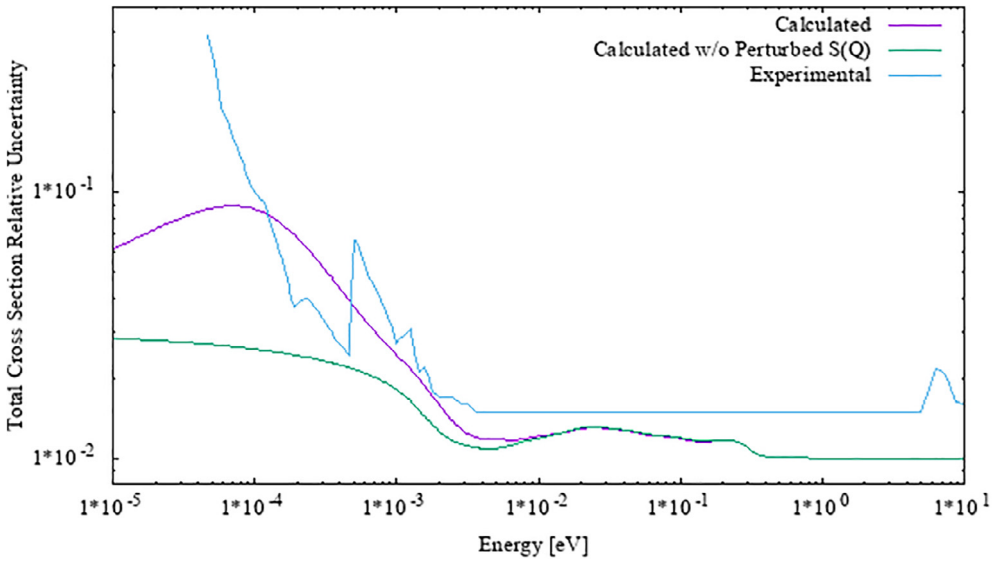

Fig. 12. Experimental and calculated uncertainty for the total cross section of D_2O, using the perturbed D in D_2O cross sections.

in (Scotta et al., 2016) – it should be noted that these results are preliminary – when calculating the uncertainties from the IKE model used in JEFF-3.1.1.

The combined calculated uncertainty for D and O in D_2O agrees quite well with the experimental uncertainty for D_2O and the set of parameter uncertainties appears to reflect the bounds of current experimental understanding well. While this was not an outcome explicitly sought, the perturbation of D_2O in this work gives a reasonable representation the total cross section uncertainty. One region that may be improved is the 0.1–1 meV region, in which the current parameter uncertainty set over-predicts the total cross section uncertainty with respect to experimental data. This region is dominated by the structure correction $S(Q)$ and the specific means of estimating uncertainties for this quantity were relatively crude.

5.2.2. Covariances for H_2O cross section

A covariance matrix for H, D and O was calculated from the tabulation of the perturbed thermal cross section files. Fig. 14 shows the correlation map for the total cross section of H_2O. Clearly, two regions are fairly distinct from each other, namely <8 meV and >8 meV and a strong anti-correlation exists between the two. This fades around 1–10 eV, as the free-atom cross section tends to dominate the effect on the cross section. Fig. 15 contains a correlation map between the total H_2O cross section and the perturbed LEAPR parameters used to construct it.

Examination the covariance data suggests that the most significant parameters to adjust are the free-atom cross section, the four main weights (diffusion, spectrum, and oscillators), oscillator energies and a small number of the Gaussian parameters. Due to the approach in perturbing the weights, there is a very strong

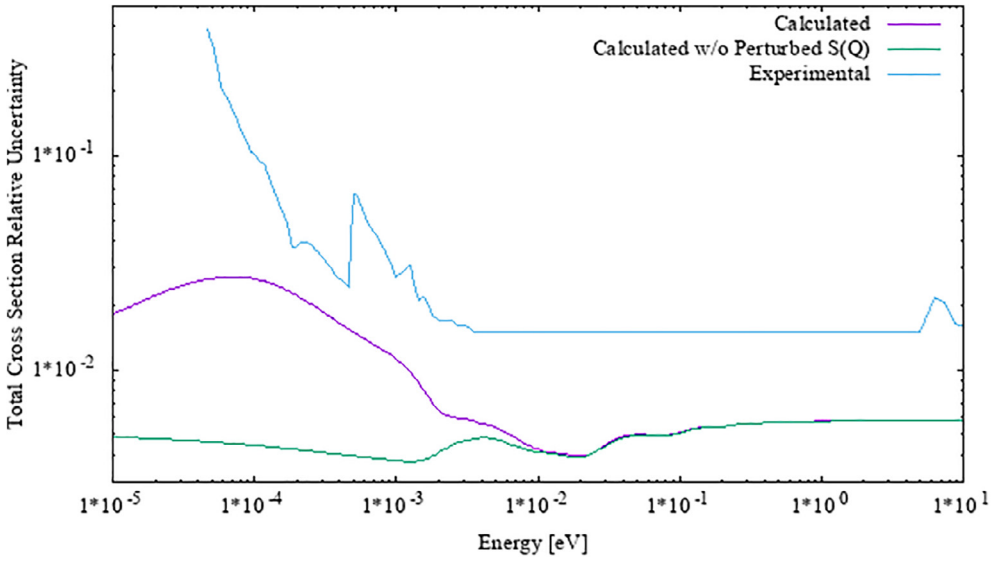

Fig. 13. Experimental and calculated uncertainty for the total cross section of D_2O, using the perturbed O in D_2O cross sections.

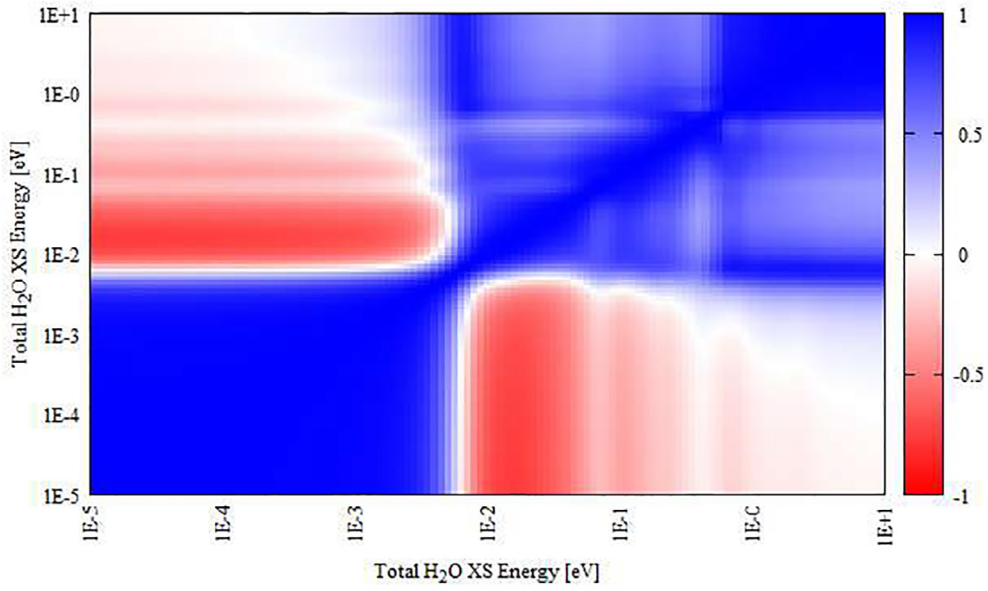

Fig. 14. Correlation map that represents the covariance matrix of the total cross section of H_2O below 1 eV.

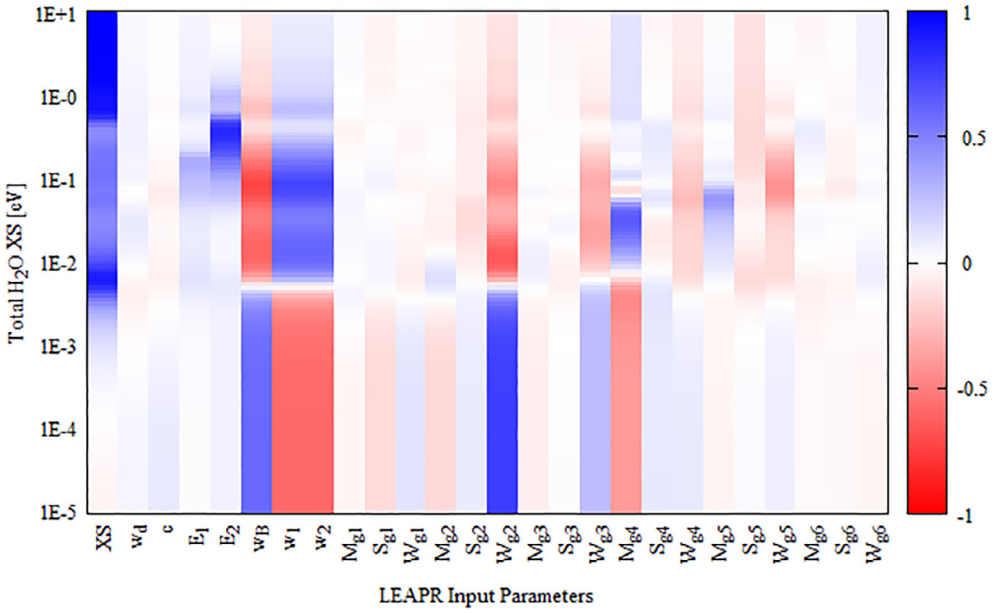

Fig. 15. Correlation map between total H_2O cross section and LEAPR input parameters. M_X, S_X and W_X refer to the mean, standard deviation and weight of each Gaussian function used to reconstruct the CFS.

anti-correlation between the spectrum and oscillator weights; the diffusion weight is much smaller in magnitude relative to the other weights and thus remains virtually independent. This behaviour is reflected in the correlations in most of the LEAPR parameters which have some dependence on the weight, namely all the Gaussian parameters and oscillator parameters. An inflection point for these correlations can be seen where the oscillator influence begins to take effect in the >8 meV range. Even with refinement of the perturbation scheme, this dependence cannot be removed owing to the requirement of all weights summing to 1. Smaller, localised effects can also be observed, such as the positive correlation of μ_4 to the cross section, implying the position of the main rotational peak will increase the total cross section if shifted forward in energy. The second oscillator energy, which is a degeneration of two vibrational modes of similar energy also appears to have a moderate influence on the higher energies, with an increase in energy resulting in an increase cross section in between 0.1 and 1 eV. This may have considerable impact on systems containing a significant ^{239}Pu inventory owing to the 0.4 eV resonance peak in the fission cross section. Other significant contributions arise from the widths and weights of the 2nd and 3rd Gaussian functions in the spectrum (<50 meV), which are observed to have anti-correlation effects in the 8 meV–0.6 eV range.

A correlation map between the total cross section and the CFS itself is shown in Fig. 16. As expected, the lower end of the CFS energy range correlates positively with the lower energy of the total cross section. At higher CFS and cross section energies, it is also observed that the correlation generally weakens to insignifi-

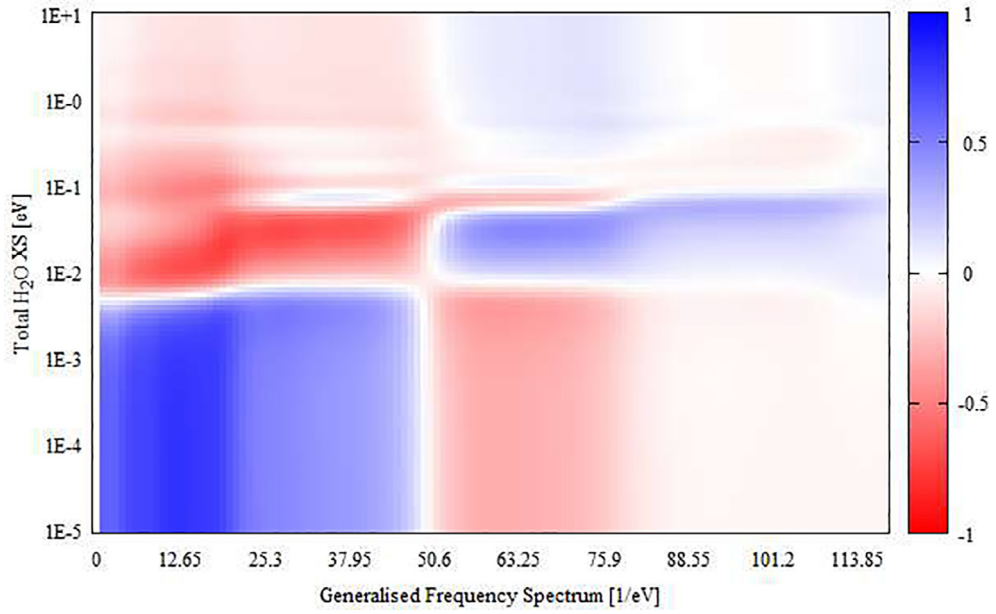

Fig. 16. Correlation map between total H_2O cross section and the GFS.

cance, which is also expected as the effect of the dynamics of the molecule diminishes with higher incident neutron energy and the tail of the rotational band tends not to impact the cross section significantly. It should also be noted that as the weight of the CFS is derived from the CFS itself, the profile of the CFS is coupled to the weights of all the modes of excitation. This point is key to understand if localised adjustments are to be make on the original data.

5.2.3. Covariances for D_2O cross section

A covariance matrix for D and O was calculated from the tabulation of the perturbed thermal cross section files. Figs. 15 and 16 show the correlation map for the total cross section of D_2O using the perturbed D and O sets of cross section.

The correlation maps for D and O in the D_2O cross section, in Figs. 17 and 18, show a weak to strong positive correlation over the entire range of energies. This denotes a fairly rigid behaviour of the cross section with respect to the parameters used to calculate it. The correlation maps for D and O in the D_2O cross section that have not had the structure correction perturbed are even more rigid, with stronger correlations in the (>0.001 eV: <0.001 eV) regions. The experimental uncertainties in the low energy region of the D_2O cross section are relatively substantial and do not extend to the end of the cold range, so it is difficult to determine whether the scheme and parameter uncertainties can potentially account for cross section uncertainty. In any case, the structure correction perturbation used in this work could be refined further and continued analysis at the MD level would provide a better description of the structure correction uncertainties. The LEAPR parameter correlations to the total cross section are shown in correlation maps in Figs. 19 and 20.

The correlations between parameters in D and O in D_2O and the total cross section are also generally weak. In the case of D in D_2O,

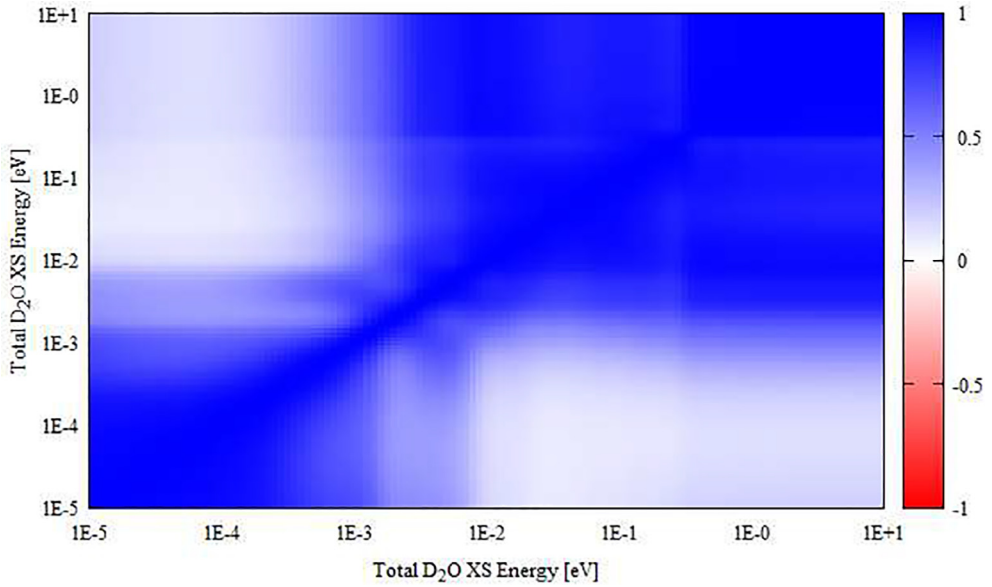

Fig. 17. Correlation map that represents the covariance matrix of the total cross section of D_2O below 1 eV when perturbing D in D_2O.

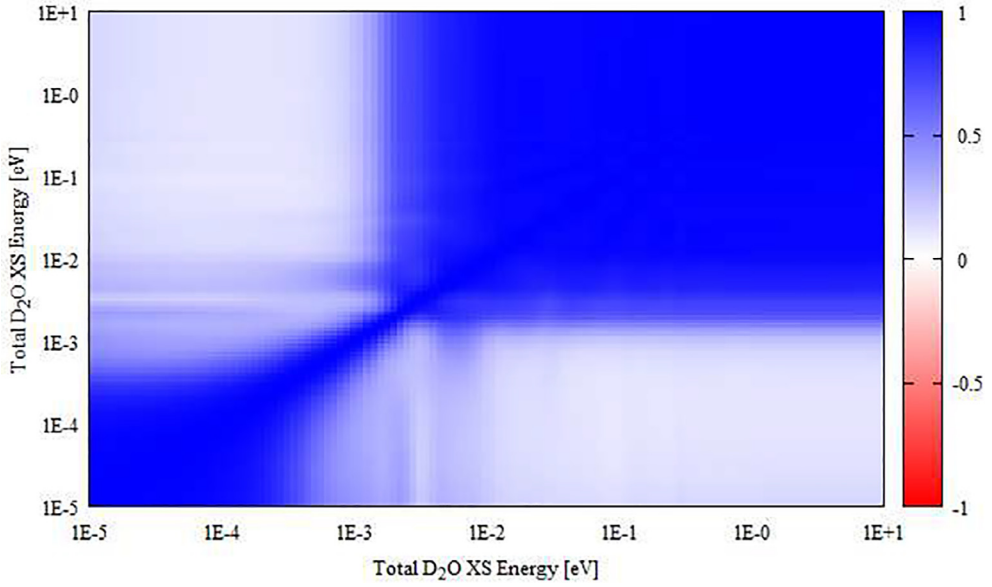

Fig. 18. Correlation map that represents the covariance matrix of the total cross section of D_2O below 1 eV when perturbing O in D_2O.

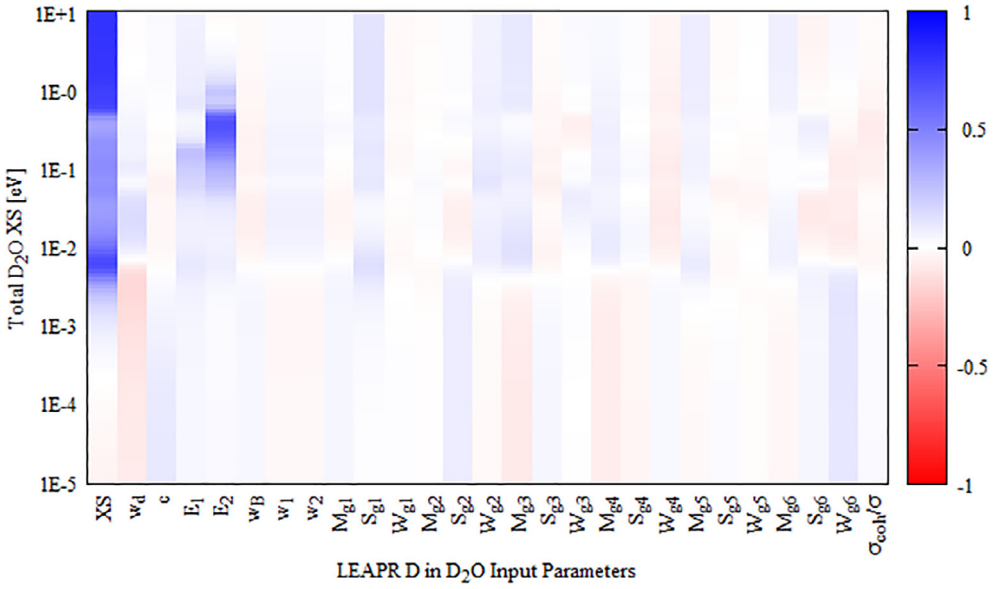

Fig. 19. Correlation map between total D_2O cross section and the D in D_2O LEAPR input parameters.

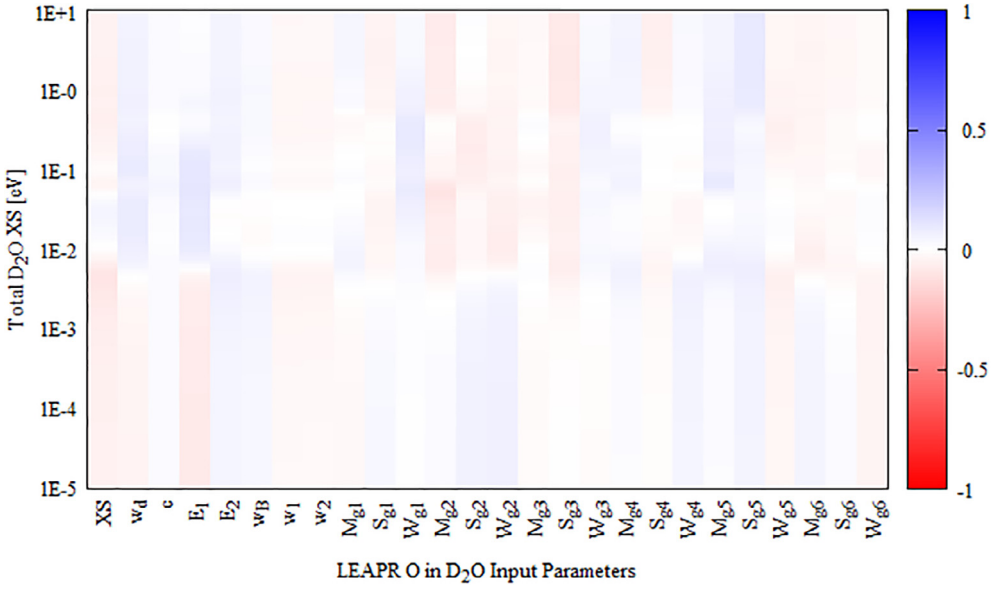

Fig. 20. Correlation map between total D_2O cross section and the O in D_2O LEAPR input parameters.

as with H_2O there is a strong correlation with the free-atom cross section and the higher energies of the total cross section and the local strong correlation between the second oscillator energy and 0.1–1 eV range of the total cross section. Also like the calculations H_2O, the coupling of the weight parameters couples most of the LEAPR parameters together. In the case of O in D_2O, the parameter correlations are all relatively weak - an expected result owing to the small impact that the O cross section has on the D_2O total cross section with respect to D.

5.3. Uncertainty propagation into the OPAL Reactor model

5.3.1. K_{eff} uncertainty

The perturbed cross sections were used in a Serpent model of the OPAL Reactor to observe the effects of the propagation of uncertainties into a real system. k_{eff} was observed for 962 separate cases (486 each with perturbed H and perturbed D & O). Figs. 21 and 22 shows the distribution of results using perturbed H_2O and D_2O files, respectively. Both datasets pass simple quartile tests for normality, however the D_2O distribution does exhibit excess kurtosis. The average k_{eff} calculated over 200 unperturbed runs was 0.99911, which falls in the centre of each distribution. Table 10 contains the computed uncertainty induced by the perturbed cross sections as calculated by Eq. (7).

While the separate effects cannot simply be summed to realised a total uncertainty, the bounds of the total moderator uncertainty with respect to the thermal cross section model parameters is likely between 46 and 85 pcm, with an RMS value of 60 pcm. The only major fissile isotope in the system is ^{235}U, with an induced uncertainty in the total fission rate of 0.015% and 0.011% for H_2O and D_2O, respectively. This corresponds to an uncertainty estimate of approximately 48 and 41 pcm for

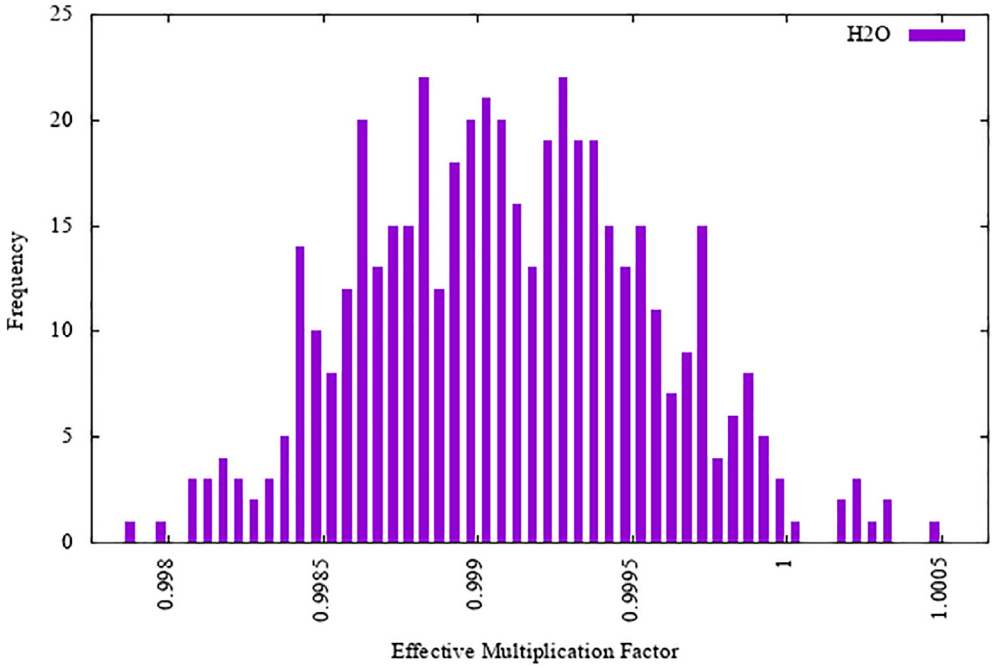

Fig. 21. k_{eff} in OPAL using perturbed H in H_2O cross section data.

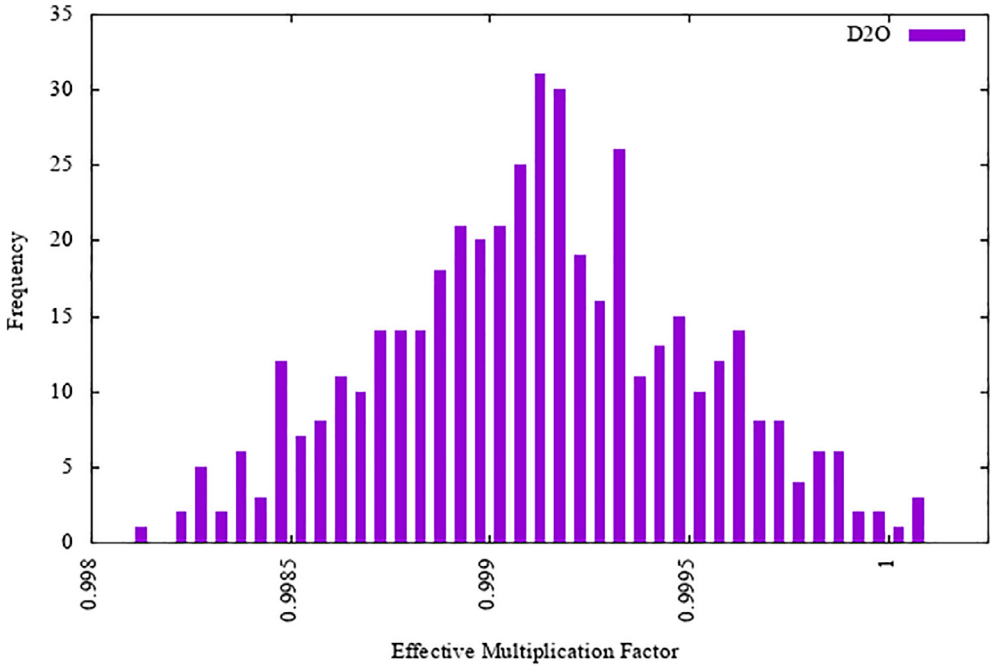

Fig. 22. k_{eff} in OPAL using perturbed D and O in D_2O cross section data.

H_2O and D_2O, respectively, which agrees with the induced errors reported in Table 10.

Table 10
Calculated uncertainties of k_{eff} in the OPAL Reactor.

	H_2O [pcm]	D_2O [pcm]
Observed Uncertainty σ_{obs}	47.2	40.0
Reported Statistical Uncertainty σ_{stat}	10.0	10.0
Unbiased Statistical Uncertainty $\sigma_{unbiased}$	10.6	10.6
Induced Uncertainty σ_{XS}	46.0	38.6

5.3.2. Flux uncertainty

The flux in various regions within the reactor facilities were calculated using detectors in Serpent. Specifically, a coarse-group thermal flux structure was used to tally the flux in the 3 fuel types, the cadmium poison wires, 3 irradiation facilities in the reflector, as well as the leakage out of the system. An epithermal and fast flux tally was also taken for each region, but as expected, the induced uncertainty was statistically insignificant. In addition, no detector result was found to be statistically significant <0.1 meV. The results obtained from the detectors are contained in Table 11 for the perturbed H_2O cross sections and Table 12 for the perturbed

Table 11
Detector results from OPAL using perturbed H_2O cross sections.

Region	0.1–10 meV	10–100 meV	0.1–1 eV	1–10 eV
Fuel Type 1	0.69%	0.14%	0.47%	0.35%
Fuel Type 2	0.92%	0.12%	0.46%	0.35%
Fuel Standard	1.02%	0.12%	0.46%	0.34%
Cadmium		0.13%		
Leakage				
Low Flux Facility				
Mid Flux Facility			0.21%	0.36%
High Flux Facility		0.16%	0.29%	0.33%

Table 12
Detector results from OPAL using perturbed D_2O cross sections.

Region	0.1–10 meV	10–100 meV	0.1–1 eV	1–10 eV
Fuel Type 1		0.06%		
Fuel Type 2		0.06%		
Fuel Standard				
Cadmium		0.15%		
Leakage				
Low Flux Facility		0.22%		0.60%
Mid Flux Facility				0.40%
High Flux Facility	0.23%	0.23%	0.15%	0.30%

D_2O cross sections. Blank entries indicate as statistically insignificant result. Red entries indicate a marginal result with an $0.5 \leq \sigma_{obs}/\sigma_{stat} \leq 0.6$.

The most statistically significant perturbation-induced uncertainty in the detectors occurs in the 10–100 meV range, which also contains the peak of the Maxwellian flux of the core. The perturbed H_2O cross sections have produced a stronger effect on the flux values of the fuel regions, not surprisingly owing to the presence of H_2O in the core. The high flux facility tally also shows a moderate sensitivity to the perturbed cross sections from both cross section sets, which is also reasonable given the proximity to the core. However, the magnitude of the uncertainties are not particularly large and likely will be negligible with respect to other uncertainties of the system.

5.3.3. Comparison to previous work

A similar propagation of uncertainty was conducted in the same OPAL reactor configuration (Maul, 2017) using perturbed H_2O data generated by Noguere et al. (2017) and Rochman and Koning (2012). The data produced by Rochman was a demonstration of the principle and the uncertainties were defined in an ad hoc way, without relation to current experimental data. As such, they produced large uncertainties in k_{eff}, with an induced error of 278 pcm, though this number is likely overestimated owing to the non-Gaussian profile of the distribution of sampled k_{eff} results. The data from Noguere produced a Gaussian distribution of k_{eff} with $\sigma_{induced} = 189$ pcm. Only scalar parameters were used in perturbing this data, which generally larger uncertainties attributed to them. Both of these cross sections were based on the IKE model used in JEFF-3.1.1.

6. Conclusion

The perturbation scheme described in this work has been used to generate uncertainties in the H_2O and D_2O cross section by sampling LEAPR parameters from distributions obtained from experimental uncertainties. 486 perturbed iterations for H in H_2O and D and O in D_2O were calculated and the uncertainties were analysed. The uncertainty of the total cross section was obtained and found to agree reasonably well with experimental uncertainties and in the case of H in H_2O, previous LEAPR parameter-based estimates of uncertainty. The key parameters that predominantly influence the total cross section are the four scalar weights associated with the different excitation modes of the dynamic structure of the molecules, and key features of the CFS, such as the rotational peak positions and translational mode profile for H in H_2O and D in D_2O. While the H_2O cross section was observed to exhibit model flexibility with respect to individual parameters, the D and O in D_2O cross sections exhibited much more rigidity with weak to strong positive covariances between each point in the cross section.

Based on these results, the scheme looks promising after some refinement to better exploit the potential, such as:

- Calculating through more iterations. 486 samples for each cross section type was suitable for an initial analysis, but with more sampling and the orthogonality approach extended to more parameters, the variability could be captured more precisely.
- Refinement of the vector quantities reconstruction. The CFS could be reconstructed from the VACF, which could be perturbed directly, or indeed parameters from the MD calculation itself could be perturbed. The partial structure factors could be analysed from an MD basis further as well.
- Interpretation of the alpha/beta grids impact on the total cross section. While the current scheme does perturb these grids, quantifying the effect is difficult and is necessarily tied to the CFS structure itself.
- Analysis examining subsets of LEAPR parameters, where applicable to better understand the dependence between variables.
- Examination of differential quantities of the cross section, rather than just the total.
- Propagation into a wider range of benchmarks, such as the International Criticality Safety Benchmark Experiment Handbook (ICSBEP) scenarios, particularly those with a plutonium inventory.

The perturbed cross sections were used in a criticality problem in the OPAL Reactor using Serpent to propagate the uncertainties to a real-world system. The effect on criticality was marginal, but statistically significant with 48 and 41 pcm uncertainty in k_{eff} induced from the perturbed H_2O and D_2O cross sections, respectively. In addition, some small uncertainties were also observed in flux tallies at various positions within the reactor. These are localised around the thermal peak in flux (10–100 meV) and primarily affected the flux in the fuelled regions (in the case of H_2O) and modestly in the high flux irradiation facility. Changes in the ^{235}U fission rate were observed at ~0.01%, which agrees with the uncertainty in k_{eff}.

Acknowledgements

This work was funded in part by the Australian Institute Nuclear Science and Engineering (AINSE). J. I. M. D acknowledges the support provided by Instituto Balseiro, CONICET and ANPCyT through project PICT-0937-2015.

References

Bellissent-Funel, M.-C., Chen, S.H., Zanotti, J.-M., 1995. Single-particle dynamics of water molecules in confined space. Phys. Rev. E 51, 4558. https://doi.org/10.1103/PhysRevE.51.4558.

Braoudakis, G., 2015. Opal nuclear reactor: reactor specification (research reactor benchmarking database: facility specification and experimental data). IAEA Tech. Rep. Series 480. IAEA.

Brown, D.A., Chadwick, M.B., Capote, R., Kahler, A.C., Trkov, A., Herman, M.W., Sonzogni, A.A., Danon, Y., Carlson, A.D., Dunn, M., Smith, D.L., Hale, G.M., Arbanas, G., Arcilla, R., Bates, C.R., Beck, B., Becker, B., Brown, F., Casperson, R.J., Conlin, J., Cullen, D.E., Descalle, M.-A., Firestone, R., Gaines, T., Guber, K.H.,

Hawari, Holmes, J., Johnson, T.D., Kawano, T., Kiedrowski, B.C., Koning, A.J., Kopecky, S., Leal, L., Lestone, J.P., Lubitz, C., Márquez Damián, J.I., Mattoon, C.M., McCutchan, E.A., Mughabghab, S., Navratil, P., Neudecker, D., Nobre, G.P.A., Noguere, G., Paris, M., Pigni, M.T., Plompen, A.J., Pritychenko, B., Pronyaev, V.G., Roubtsov, D., Rochman, D., Romano, P., Schillebeeckx, P., Simakov, S., Sin, M., Sirakov, I., Sleaford, B., Sobes, V., Soukhovitskii, E.S., Stetcu, I., Talou, P., Thompson, I., van der Marck, S., Welser-Sherrill, L., Wiarda, D., White, M., Wormald, J.L., Wright, R.Q., Zerkle, M., Žerovnik, G., Zhu, Y., . ENDF/B-VIII.0: the 8th major release of the nuclear reaction data library with CIELO-project cross sections, new standards and thermal scattering data. Nucl. Data Sheets, Special Issue on Nuclear Reaction Data 148, 1–142. https://doi.org/10.1016/j.nds.2018.02.001.

Dritsa, M., Kostikas, A., 1967. Total Cross Section of Water at Room Temperature and 200 Degrees C (No. 63L), Report from Misc. OECD Countries to EANDC. France.

Dritsa, S., Gaitanis, N., 1967. Total Neutron Cross Section of D2O. (No. 87), Report from Misc. OECD Countries to EANDC. France.

Egelstaff, P.A., Schofield, P., 1962. On the evaluation of the thermal neutron scattering law. Nucl. Sci. Eng. 12, 260–270.

González, M.A., Abascal, J.L.F., 2011. A flexible model for water based on TIP4P/2005. J. Chem. Phys. 135, 224516–224516-8. https://doi.org/10.1063/1.3663219.

Haywood, B.C., Thorson, I., 1962. The Scattering Law for Light and Heavy Water at 20 C and 150 C., in: Proceedings of the Brookhaven Conference on Neutron Thermalization. Presented at the Brookhaven Conference on Neutron Thermalization, IAEA.

Heinloth, K., 1961. Subthermal neutron scattering on H2O, CH2O2 and C6H6. Zeitchrift Phys. 163, 218.

Koppel, J.U., Houston, D.H., 1978. Reference Manual for ENDF Thermal Neutron Scattering Data, GA-8774.

Koppel, J.U., Young, J.A., 1965. The role of interference scattering in neutron thermalization by heavy water. Nukl. West Ger. Discontin. 12 Vol, 7.

Kropff, F., Latorre, J.R., Granada, J.R., Castro Madero, C., 1975. New measurement of the total neutron cross section of D2O at 20C between 0.0005 and 10 eV.

Lappi, S.E., Smith, B., Franzen, S., 2004. Infrared spectra of H216O, H218O and D2O in the liquid phase by single-pass attenuated total internal reflection spectroscopy. Spectrochim. Acta. A. Mol. Biomol. Spectrosc. 60, 2611–2619. https://doi.org/10.1016/j.saa.2003.12.042.

Leppänen, J., Pusa, M., Viitanen, T., Valtavirta, V., Kaltiaisenaho, T., 2015. The Serpent Monte Carlo code: Status, development and applications in 2013. Ann. Nucl. Energy 82, 142–150. https://doi.org/10.1016/j.anucene.2014.08.024.

MacFarlane, R.E., 1994. New thermal neutron scattering files for ENDF/B-VI release, 2.

Márquez Damián, J.I., Granada, J.R., Malaspina, D.C., 2014. CAB models for water: a new evaluation of the thermal neutron scattering laws for light and heavy water in ENDF-6 format. Ann. Nucl. Energy 65, 280–289. https://doi.org/10.1016/j.anucene.2013.11.014.

Marquez Damian, J.I., Granada, R., Baxter, D., Parnell, S., C Evans, D., 2015. Measurement of the total cross section of heavy water in the 0.1 meV–1 eV energy range at 20 and 50 degrees C 38. https://doi.org/10.1393/ncc/i2015-15178-x

Marquez Damian, J.I., Malaspina, D.C., Granada, J.R., 2013. Vibrational spectra of light and heavy water with application to neutron cross section calculations. J. Chem. Phys. 139, 024504–024504-6. https://doi.org/10.1063/1.4812828.

Marti, J., Padró, J.A., Guàrdia, E., 1994. Molecular dynamics calculation of the infrared spectra in liquid H2O–D2O mixtures. J. Mol. Liq. 62, 17–31. https://doi.org/10.1016/0167-7322(94)00769-1.

Mattes, Keinert, 2005. Thermal Neutron Scattering Data for the Moderator Materials H2O, D2O and ZrHx in ENDF-6 Format and as ACE Library for MCNP(X) Codes. IKE, Germany.

Maul, L., 2017. Impact of Perturbed H2O Thermal Scattering Data in OPAL Reactor Calculations. Proceedings of M&C, Presented at the M&C 2017, Jeju Korea.

Muir, D.W., Boicourt, R.M., Kahler, A.C., 2012. The NJOY Nuclear Data Processing System, Version 2012 (No. LA-UR-12-27079), The NJOY Nuclear Data Processing System. LosAlamos National Laboratory.

Nelkin, M., 1960. Scattering of slow neutrons by water. Phys. Rev. 119, 741. https://doi.org/10.1103/PhysRev. 119.741.

Noguere, G., Scotta, J.P., De Saint Jean, C., Archier, P., 2017. Covariance matrices of the hydrogen neutron cross sections bound in light water for the JEFF-3.1.1 neutron library. Ann. Nucl. Energy 104, 132–145. https://doi.org/10.1016/j.anucene.2017.01.044.

Novikov, A., Van'kov, A., Gosteva, L., 1990. Temperature dependence of the general spectrum for water. J. Struct. Chem. 31, 77–85. https://doi.org/10.1007/BF00752017.

Parks, D.E. (Ed.), 1970. Slow neutron scattering and thermalization, with reactor applications. W. A. Benjamin, New York.

Rochman, D., Koning, A.J., 2012. Random adjustment of the H in H2O neutron thermal scattering data. Nucl. Sci. Eng. 172, 287–299.

Rochman, D., Zwermann, W., van der Marck, S.C., Koning, A.J., Sjöstrand, H., Helgesson, P., Krzykacz-Hausmann, B., 2014. Efficient use of monte carlo: uncertainty propagation. Nucl. Sci. Eng. 177, 337–349 https://doi.org/10.13182/NSE13-32.

Russell Jr, J., Neill, J.M., Brown, J.R., 1966. Total cross section measurements in H2O. (General Atomic Division Reports No 1966 7581).

Scotta, J.P., Noguere, G., Marquez Damian, J.I., 2016. Towards a Covariance Matrix of CAB Model Parameters for H (H2O). Data for Science and Technology.

Sköld, K., 1967. Small energy transfer scattering of cold neutrons from liquid argon. Phys. Rev. Lett. 19, 1023. https://doi.org/10.1103/PhysRevLett. 19.1023.

Soper, A.K., Benmore, C.J., 2008. Quantum differences between heavy and light water. Phys. Rev. Lett. 101,. https://doi.org/10.1103/PhysRevLett. 101.065502 065502.

Vineyard, G.H., 1958. Scattering of slow neutrons by a liquid. Phys. Rev. 110, 999. https://doi.org/10.1103/PhysRev.110.999.

Yoshida, K., Matubayasi, N., Nakahara, M., 2008. Self-diffusion coefficients for water and organic solvents at high temperatures along the coexistence curve. J. Chem. Phys. 129,. https://doi.org/10.1063/1.3006420 214501.

Zaitsev, K.N., Petrov, V.N., Kuznetsov, S.P., Langer, O.A., Meshkov, I.V., Perekrestenko, A.D., 1991. The total cross sections of the interaction of ultracold neutrons with H2O and D2O. At. Energy 70, 238–242. https://doi.org/10.1007/BF01126475.